Encapsulation of SnO_2 nanoparticles into hollow TiO_2 nanowires as high performance anode materials for lithium ion batteries

Qinghua Tian [a], Zhengxi Zhang [a,*], Li Yang [a,*], Shin-ichi Hirano [b]
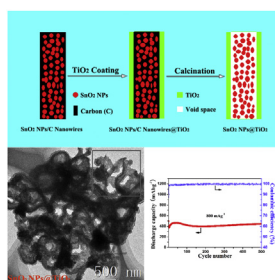
[a] School of Chemistry and Chemical Engineering, Shanghai Jiao Tong University, Shanghai 200240, PR China
[b] Hirano Institute for Materials Innovation, Shanghai Jiao Tong University, Shanghai 200240, PR China

HIGHLIGHTS

- We fabricated a new morphological nanostructure of composite: encapsulation of SnO_2 nanoparticles into hollow TiO_2 nanowires.
- The composite realized the integration of the high capacity SnO_2 and structural stability TiO_2.
- This nanostructure made the composite to have sufficient physical buffer ability.
- The composite exhibited good lithium storage performance and excellent cyclability.

GRAPHICAL ABSTRACT

ARTICLE INFO

ABSTRACT

In this work, a new nanostructure of SnO_2 nanoparticles (NPs) encapsulated into hollow TiO_2 nanowires ($SnO_2@TiO_2$) has been successfully fabricated. This unique architecture intrinsically possess void space in between the TiO_2 shell and SnO_2 nanoparticle cores, as confirmed by XRD, XPS, SEM, TEM and HRTEM characterizations. The TiO_2 shell of the composite can not only alleviate the pulverization and drastic volume change of the SnO_2 NPs and maintain the structural integrity, but also contribute to the total capacity of the composite. Moreover, the void space can also accommodate the volume expansion of SnO_2 and provide highly efficient channels for the fast transport of both electrons and lithium ion during discharge/charge cycling process. When tested as potential anode materials for lithium ion batteries, the as-prepared hollow TiO_2 nanowires shell encapsulating SnO_2 NPs architecture exhibits good lithium storage performance and excellent cyclability (which delivers a higher reversible capacity of 445 mAh g^{-1} at 800 mA g^{-1} after 500 cycles). The unique architecture should be responsible for the superior electrochemical performance.

1. Introduction

Currently, lithium ion batteries (LIBs) predominantly use graphite as anode materials, which cannot meet the increasing demand for powering electric vehicles (EVs) or hybrid electric vehicles (HEVs) energy storage requirements due to the low theoretical capacity of around 372 mAh g^{-1} [1,2]. Therefore, it is highly desirable to develop alternative anode materials to meet the need for next-generation LIBs.

As the most promising candidates for anode materials, transition metal oxides with high capacities from 700 to 1000 mAh g^{-1} have been widely investigated to replace the commercial graphite anode for LIBs in the past decade [3,4]. Among them, Tin dioxide (SnO_2) is one of the most-studied anode materials because of its

* Corresponding authors. Tel.: +86 21 54748917; fax: +86 21 54741297.
E-mail address: liyangce@sjtu.edu.cn (L. Yang).

high theoretical capacity, safe working potential and environmental benignity [5,6]. Despite the high theoretical capacity, however, the practical use of the SnO_2-based anode materials is greatly hampered by their quick capacity fading upon an extended number of cycles, which is believed to be caused by the huge volume change of SnO_2 during discharge/charge process [7]. Meanwhile, the electron conductivity of SnO_2 is poor. To mitigate these problems, several strategies have been proposed and improved the lithium storage performance. For example, one of the well-known methods is to design various SnO_2 nanostructures with large surface area and high surface-to-volume ratio, such as nanotubes [8], nanoboxes [9], nanosheets [10] and/or porous nanostructures; other widely practiced strategy is to improve the conductivity of SnO_2-based materials by combing them with electronically conductive agents, such as CNTs, graphene and noble metals [11–15]. Unfortunately, SnO_2 and/or SnO_2-based composites with considerable capacity fading still exist upon cycling in both strategies. Because these SnO_2 nanostructures are inclined to breaking down, aggregation and pulverization during cycles and the SnO_2 nanoparticles are loosely attached to CNTs [16,17]. In addition to SnO_2, titanium dioxide (TiO_2) is also considered as one of the most-studied anode materials, owing to its long cycle life, better safety, higher structural stability, low cost and environmentally benign [18]. Despite the above inherent beneficial characteristics, there are still obstacles that hinder the further development of TiO_2-based anode materials for LIBs, especially the relatively low electronic conductivities and low practical capacity (ca. 170 mAh g^{-1}) [19].

Recently, efforts for combining SnO_2 and other electrochemically active metal oxides to obtain a composite with excellent electrochemical performance have been reported, that owing to the synergistic effects between the SnO_2 and other oxides [1,20,21]. For example, SnO_2/TiO_2 nano-heterostructures have been recently suggested to overcome the demerits of both materials, and to improve the electrode performance [22]. TiO_2 with neglectable volume change (3–4%), encapsulating SnO_2 NPs can be used as the stable barrier to effectively maintain the mechanical integrity of SnO_2 during the reaction with lithium ions. At the same time, the low specific capacity of TiO_2 can be compensated by the high capacity of SnO_2. Moreover, a nanotubular hollow type is more suitable for accommodating volume expansion and thus enabling better cycle performance than the nanoparticle type [23]. Herein, the hollow TiO_2 nanowires can not only facilitate the lithium transport, but also work as a mechanical support which can effectively buffer the volume change of tin (Sn) and prevent the tin crystals from agglomerating during cycling. Finally, a composite with excellent electrochemical performance could be obtained, owing to the synergistic effects between the SnO_2 and TiO_2.

In this study, hollow TiO_2 nanowires encapsulating SnO_2 nanoparticles (NPs) was fabricated by template-assisted hydrolysis and condensation of tetrabutyl titanate (TBOT), and subsequent calcination in air. The SnO_2 NPs/carbon (C) nanowires (NWs) were used as templates and prepared with pyrrole *in situ* polymerization coating SnO_2 NPs in aqueous solution, followed by a carbonized transformation process. To our knowledge, this is the first report on fabricating this unique structure with hollow TiO_2 nanowires shell encapsulating SnO_2 NPs, which intrinsically possess void space in between the TiO_2 shell and SnO_2 NPs cores. The TiO_2 shell of $SnO_2@TiO_2$ composite can alleviate the pulverization and drastic volume change of the SnO_2 NPs and maintain the structural integrity. The void space can also accommodate the volume expansion of SnO_2 and provide highly efficient channels for the fast transport of both electrons and lithium ion during discharge/charge cycling process. The designed hollow TiO_2 nanowires shell encapsulating SnO_2 NPs architecture exhibits good lithium storage performance and excellent cyclability.

2. Experimental section

2.1. Preparation of samples

2.1.1. Preparation of SnO_2 NPs

SnO_2 NPs were synthesized by a modified approach that was similar to reference [10]. Briefly, 0.213 g tin dichloride dehydrate (AR, Aldrich) was added to 60 mL mixed solvent of distilled water and ethanol with the volume ratio being 1:1. After stirred for 30 min, followed by the addition of 1.68 g ammonium hydroxide (25–28 wt%). This suspension was transferred into a 100 mL teflon-line stainless autoclave after stirred for 10 min, and then placed in an oven at 120 °C for 6 h. The autoclave used an ice-water bath to rapid cooling after the reaction finished. The products were collected by centrifugation and washed with distilled water and ethanol thoroughly, and then dried in a vacuum oven at 60 °C overnight, followed by calcination in a Muffle furnace at 400 °C for 3 h under air at a ramping rate of 0.5 °C min^{-1}, the SnO_2 NPs were obtained.

2.1.2. Preparation of SnO_2 NPs/C nanowires

100 mg as-prepared SnO_2 NPs were dispersed in 100 mL distilled water containing 60 mg cetyl trimethyl ammonium bromide (CTAB). After sonication for 30 min, 200 μL of pyrrole (99.7%, Aldrich) was added into above suspension, followed by stirred for 1 h. And then 20 mL 0.26 M ammonium persulfate aqueous solution was slowly dropped into above solution. The polymerization process was kept under stirring for 4 h at room temperature. After polymerization process finished, the black products were collected by centrifugation and washed with distilled water and ethanol thoroughly, and then dried in a vacuum oven at 60 °C overnight, followed by a carbonization in a tube furnace at 500 °C for 3 h under Ar at a ramping rate of 0.5 °C min^{-1}, the SnO_2 NPs/C NWs were obtained.

2.1.3. Preparation of hollow TiO_2 nanowires encapsulated SnO_2 nanoparticles ($SnO_2@TiO_2$)

A typical preparation process was as follows: 100 mg as-prepared SnO_2 NPs/C NWs were dispersed in absolute ethanol (134 mL), and mixed with concentrated ammonia solution (0.6 mL, 25–28 wt%) under ultrasound for 10 min. Afterward, 1.0 mL of TBOT was added dropwise in 5 min, and the reaction was allowed to proceed for ca. 3 h at 45 °C under continuous mechanical stirring. The resultant products (SnO_2 NPs/C NWs@TiO_2) were collected by centrifugation and washed with distilled water and ethanol thoroughly, and then dried in a vacuum oven at 60 °C overnight, followed by calcination in a Muffle furnace at 400 °C for 2 h under air at a ramping rate of 0.5 °C min^{-1}. Finally, the white $SnO_2@TiO_2$ was obtained.

2.2. Structure and electrochemical characterization

The morphology and microstructure of the products were obtained using field emission scanning electron microscopy (FE-SEM, JEOL JSM-7401F), high resolution transmission electron microscopy (HRTEM, JEOL JEM-2010) and transmission electron microscopy (TEM, JEOL JEM-2010) with an energy dispersive X-ray spectrometer (EDX) and a selected area electron diffraction pattern (SAED). The composition and crystal structure were characterized by X-ray diffraction measurement (XRD, Rigaku, D/max-Rbusing Cu Kα radiation). Thermogravimetric analysis (TGA) of the as-prepared $SnO_2@TiO_2$ was carried out with a thermogravimetric analysis instrument (TGA, SDT Q600 V8.2 Build 100). X-ray photoelectron spectroscopy (XPS) experiments were carried out on an AXIS ULTRA
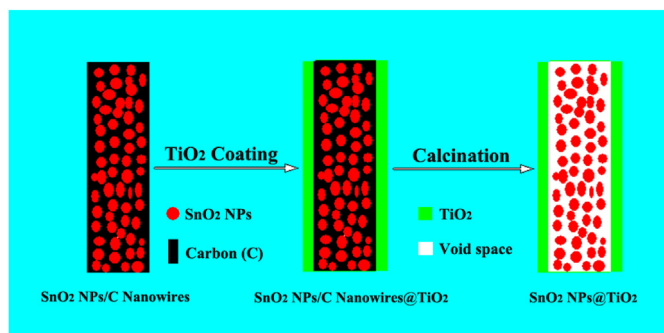
Fig. 1. Schematic illustration of the fabrication process of $SnO_2@TiO_2$ composite.

DLD instrument, using aluminum Kα X-ray radiation during XPS analysis.

Electrochemical measurements were performed using 2016-type coin cells assembled in an argon-filled glove box (German, M. Braun Co., $[O_2] < 1$ ppm, $[H_2O] < 1$ ppm). The working electrodes were composed of the active material ($SnO_2@TiO_2$), conductive material (acetylene black, AB), and binder (poly-vinyl-difluoride, PVDF) in a weight ratio of $SnO_2@TiO_2/AB/PVDF = 80:10:10$ and pasted on Cu foil. Pure lithium foil was used as the counter electrode. A glass fiber (GF/A) from Whatman was used as the separator. The electrolyte consisted of a solution of 1 M $LiPF_6$ in ethylene carbonate and dimethyl carbonate (EC + DMC) (1:1 in volume). The galvanostatic discharge/charge cycles were

carried out on a CT2001a cell test instrument (LAND Electronic Co.) over a voltage range of 0.01–3.00 V at room temperature. Cyclic voltammetry (CV) was implemented on a CHI660D electrochemical workstation. For $SnO_2@TiO_2$ composite working electrode, all the specific capacities reported and current densities used were based on the total weight of $SnO_2@TiO_2$ composite.

3. Results and discussion

The fabrication of $SnO_2@TiO_2$ composite was schematically illustrated in Fig. 1. The templates of SnO_2 NPs/C nanowires (NWs) first synthesized by pyrrole *in situ* polymerization coating SnO_2 NPs in aqueous solution, followed by a carbonized transformation process. The as-prepared SnO_2 NPs/C NWs had curved wires-like shape with a diameter distribution of ca. 200 nm (Fig. S1c). The SnO_2 NPs distributed in carbon NWs had a size distribution of ca. 15 nm (Fig. S1a, b). After the SnO_2 NPs/C NWs were coated by TiO_2, and subsequent removal of the carbon by calcination in air, the $SnO_2@TiO_2$ composite was obtained. The templates were effectively removed by calcination and the thermogravimetric (TG) (Fig. S1d) analysis of $SnO_2@TiO_2$ composite indicated that only ca. 3.5% weight loss was observed (mainly due to the evaporation of the weakly adsorbed water and trace carbon) and no observation of distinct regions of weight loss of carbon between 200 and 600 °C (this region of weight loss is mainly due to removal of carbon [24]).

We observed the morphological, structural, and compositional characterizations of the $SnO_2@TiO_2$ composite by SEM, TEM and XRD. As can be seen from Fig. 2a, b that $SnO_2@TiO_2$ composite
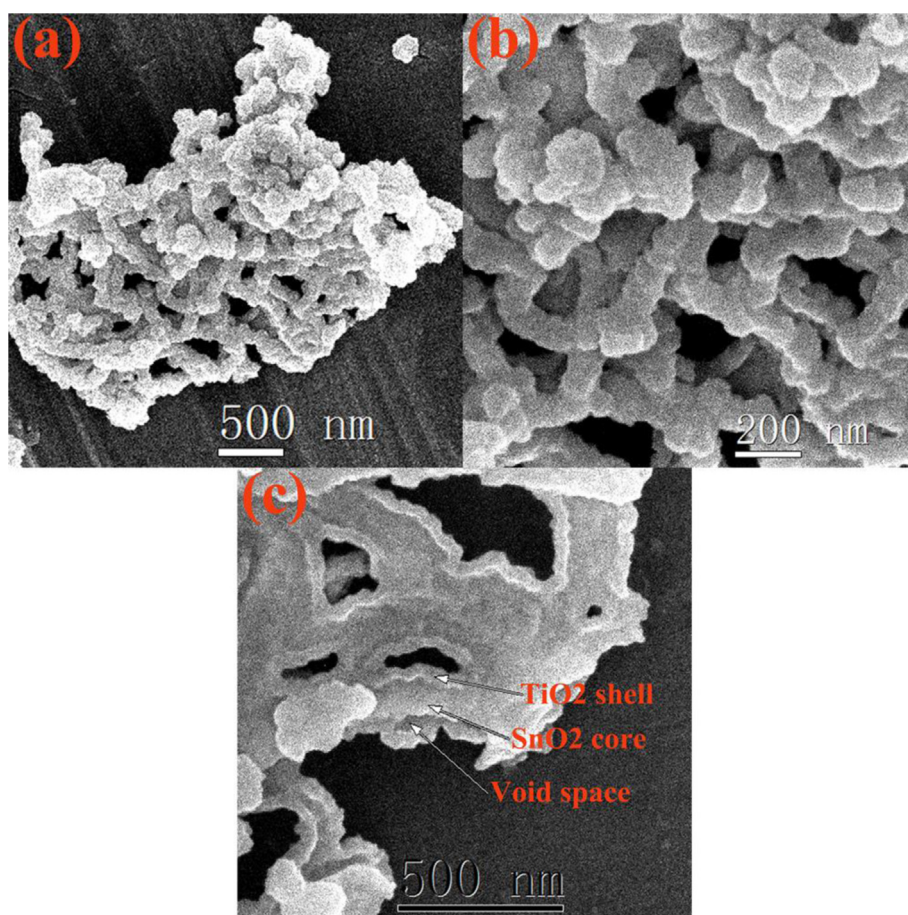

Fig. 2. FSEM images of $SnO_2@TiO_2$ composite: (a) SEM image, (b) magnified SEM image and (c) SEM image of broken or incomplete $SnO_2@TiO_2$ composite.

maintained the 1D nanostructure after the removal of carbon by SnO_2 NPs/C NWs@TiO_2 composite calcination in air, and further confirmed by the TEM shown in Fig. 3a. Interestingly, the removal of carbon layer close contact to TiO_2 layer, leading to the formation of void space between the core and shell (Fig. 3b), and fabricating the unique architecture with hollow TiO_2 nanowires shell encapsulating SnO_2 NPs cores. This phenomenon suggests that the carbon layer which directly contact to TiO_2 coating layer contains less SnO_2 NPs contents than inner carbon, and more space left than inner region when carbon removed. TEM observation (Fig. 3b, c) clearly indicates that the 1D nanostructure possess a unique yolk-shell structure, where SnO_2 NPs encapsulated in hollow TiO_2 nanowires shell (Fig. 3c). It is clearly seen from Fig. 3c that this composite possesses a compact shell (dark-colored) and a loose core (relatively bright-colored). The mean thickness of the shell is estimated to be around ca. 25 nm. Furthermore, the hollow nanowires shelled structure is also verified from the broken or incomplete SnO_2@TiO_2 composite (Fig. 2c). It shows that the distinct void space exists between the core and shell, and with a size of ca. 30 nm (indicated by white arrows in Fig. 2c). HRTEM image (Fig. 3d) of the part indicated by a square in Fig. 3c clearly shows that the visible set of lattice fringes with d-spacing of 0.26 and 0.23 nm are the characteristic of (101) and (004) lattice planes of the rutile SnO_2 and anatase TiO_2 structure, respectively. As observed from Fig. 3c, d that the SnO_2 and TiO_2 located in the core region and shell region of the SnO_2@TiO_2 composite, respectively. In addition, selected-area electron diffraction (SAED) patterns were recorded by focusing the electron beam on an area indicated by a square in Fig. 3c,

indicating the polycrystalline nature (inset of Fig. 3c). It is consistent with the polycrystalline nature of rutile SnO_2 and anatase TiO_2.

Fig. 4a reveals chemical in formation on the as-prepared SnO_2@TiO_2 composite via energy dispersive X-ray (EDX) spectra. These composite mainly include the elements Ti, O, and Sn, except for trace C and Cu come from micro-grid used as the sample stage in TEM measurements. And the Ti, O, Sn content estimated from EDX analysis is found to be 13.84, 15.97, 29.40 and 11.06, 38.20, 9.48 by weight (%) and atomic (%), respectively (top of Fig. 4a). The results are consistent with chemical in formation of SnO_2 and TiO_2. Thus, the SnO_2@TiO_2 composite contains about 61.80 (wt%) of SnO_2 and 38.2 (wt%) of TiO_2 according to the EDX analysis. The crystallographic structure of the SnO_2@TiO_2 composite was further characterized by using X-ray diffraction (XRD) shown in Fig. 4b. It is clear from the pattern of SnO_2@TiO_2 that all intensive peaks can be well indexed to anatase TiO_2 marked by squares (■) (JCPDS card no. 21-1272, S.G.: $I4_1$/amd, $a_o = 3.7852$ Å, $c_o = 9.5139$ Å) and rutile SnO_2 marked by circles (●) (JCPDS card no. 41-1445, S.G.: $P4_2$/mnm, $a_o = 4.738$ Å, $c_o = 3.187$ Å), respectively [25,26]. It is in good agreement with the TEM and SAED results.

A typical XPS spectrum for the SnO_2@TiO_2 composite is shown in Fig. 5a. Obvious Ti 2p, Sn 3d and O 1s are detected, and their high-resolution spectra are shown in Fig. 5b–d, respectively. The O 1s spectrum (Fig. 5b) for SnO_2@TiO_2 composite comprises two peaks with binding energies (BEs) of 530.3 eV and 531 eV, which are well attributable to O^{2-} in TiO_2 and SnO_2, respectively [27,28]. The high-resolution spectrum of Ti 2p shows the binding energies for Ti $2p_{3/2}$ at 458.8 eV and Ti $2p_{1/2}$ at 464.6 eV (Fig. 5c) which are
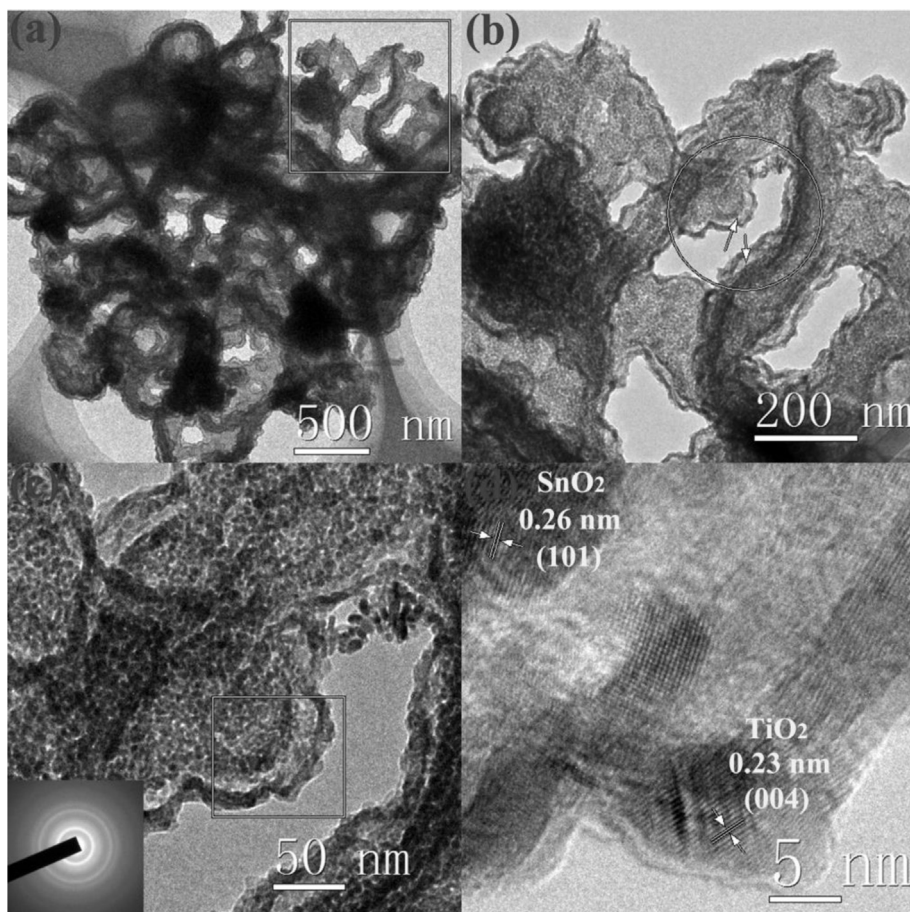

Fig. 3. TEM images of SnO_2@TiO_2 composite: (a) TEM image, (b) magnified TEM image of the part indicated by a square in (a), (c) magnified TEM image of the part indicated by a circle in (b) and SAED pattern (inset), (d) HRTEM image of the part indicated by a square in (c).
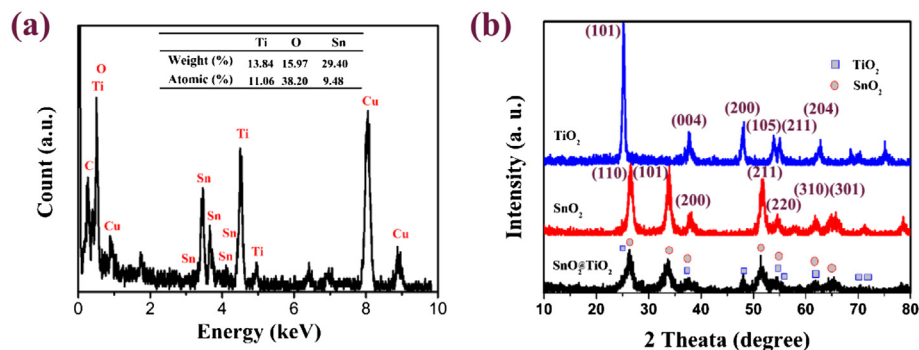
Fig. 4. EDX spectrum and XRD pattern of SnO$_2$@TiO$_2$ composite: (a) EDX spectrum, (b) XRD pattern.

assigned to Ti^{4+} in TiO$_2$ [27]. Fig. 5d shows the high-resolution spectrum of Sn 3d, the binding energies of Sn 3d$_{5/2}$ and Sn 3d$_{3/2}$ are centered at 486.7 eV and 495.1 eV which are assigned to Sn^{4+} in SnO$_2$ [29]. The analysis results from XPS further confirm that we have successfully fabricated a unique architecture consists of hollow TiO$_2$ nanowires shell and SnO$_2$ NPs cores (SnO$_2$@TiO$_2$).

Fig. 6a shows the initial five CV curves of the SnO$_2$@TiO$_2$ composite at a scan of 0.5 mV s^{-1} from 0.0 to 3.0 V. Two pair of redox peaks (cathodic, anodic) can be clearly observed. The first dominant pair shown at the potential (V) of (0.008, 0.65) can be attributed to the alloying (cathodic scan) and dealloying (anodic scan) process. In addition, the first pair is much more pronounced than the subsequent second pair, making its major contribution to the total capacity of the electrode. The second pair locating at (0.70, 1.56), and is believed to be related to the irreversible reduction of SnO$_2$ to Sn and the formation of a solid electrolyte interface (SEI) layer. This

reduction peak locating at 0.70 V shows a significantly drop in current after the first cycle correspond to the conversion reaction only. The charge–discharge voltage profiles of the as-prepared SnO$_2$@TiO$_2$ for the 1st, 2nd, 5th, 10th and 20th cycles shown in Fig. 6b. In agreement with the above CV behavior, two slope regions can be identified in the discharge process of the first cycle. Additionally, another small pair of redox peak at (1.75, 2.1) may possibly be ascribed to the lithium ion insertion into/extraction out of TiO$_2$ [1]. Therefore, TiO$_2$ not only does the supporting function in the composite alleviates the pulverization and drastic volume change of the SnO$_2$ NPs, but also contributes to the total capacity of the composite. Fig. 6b shows the charge-discharge voltage profiles of the SnO$_2$@TiO$_2$ composite measured at a current density of 800 mA g^{-1}, delivering a discharge and charge capacities of 1174 and 549 mAh g^{-1} (throughout this work, the specific capacity of the SnO$_2$@TiO$_2$ composite calculated based on its total mass),
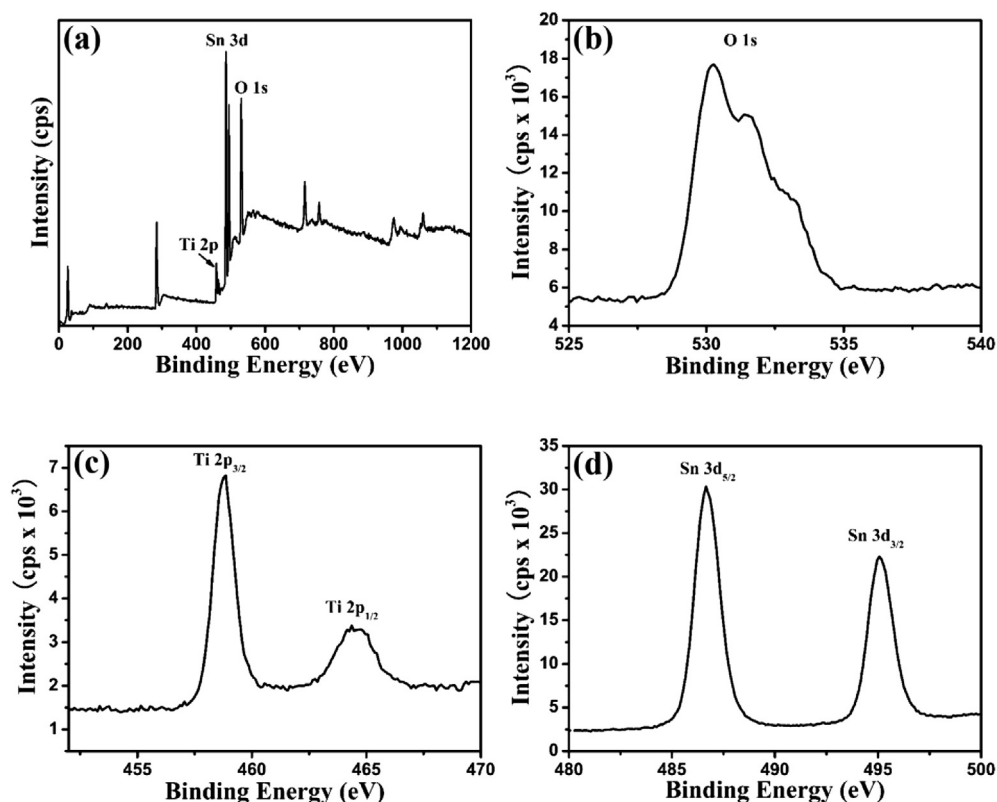

Fig. 5. XPS spectra for SnO$_2$@TiO$_2$ composite: (a) survey spectrum and high-resolution (b) O 1s, (c) Ti 2p, and (d) Sn 3d spectra.

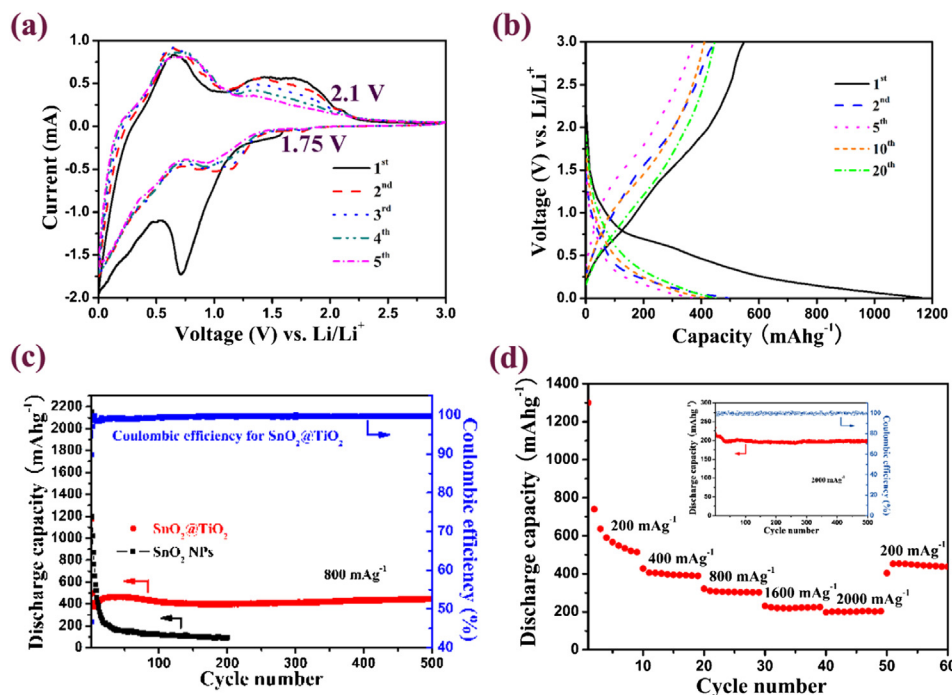**Fig. 6.** Electrochemical characterizations of the SnO$_2$@TiO$_2$ composite: (a) representative CVs at a scan rate of 0.5 mV s^{-1} between 0.0 V and 3.0 V; (b) charge/discharge voltage profiles at 800 mA g^{-1} between 0.01 V and 3.0 V; (c) comparative cycling performance between SnO$_2$@TiO$_2$ composite and SnO$_2$ NPs at 800 mA g^{-1} between 0.01 V and 3.0 V; (d) rate capabilities of the SnO$_2$@TiO$_2$ composite and cycling performance at 2000 mA g^{-1} after rate test (inset).

respectively, and giving rise to a Coulombic efficiency of 46.8%. Compared to SnO$_2$ NPs (the first discharge and charge capacities are 2156 and 1124 mAh g^{-1}, respectively, shown in Fig. 6c), the lower Coulombic efficiency and first discharge and charge capacities of SnO$_2$@TiO$_2$ are mainly attributable to the lower theoretical capacity of TiO$_2$ and the formation of Li$_2$O and a thick SEI layer on the electrode [30]. The discharge and charge capacities in the second cycle are 495, 445 mAh g^{-1}, respectively, resulting in an increased efficiency value of 89.8%. Moreover, the efficiency further increases up to 99.1% in the 24th cycle and still maintains at around 99.1% in the following cycles shown in Fig. 6e. It is worth noting that the discharge curves in the following cycles almost overlapped with the first one, showing a good cycling performance of the SnO$_2$@TiO$_2$ composite.

Fig. 6c shows the comparison of cycling performance between SnO$_2$@TiO$_2$ composite and SnO$_2$ NPs between 0.01 and 3.0 V at a current density of 800 mA g^{-1}. In Fig. 6c, the SnO$_2$ NPs with fast capacity fading can be observed during discharge/charge cycles, ascribe to their aggregation and pulverization [16]. In sharp contrast, the as-prepared SnO$_2$@TiO$_2$ composite exhibits significantly improved cycling performance (Fig. 6c). More importantly, it retains a reversible discharge capacity of 445 mAh g^{-1} even after 500 cycles, and with a Coulombic efficiency of 99.7% clearly shown in Fig. 6c. Unfortunately, for the SnO$_2$ NPs, only 95 mAh g^{-1} is retained after 500 cycles at the same current density (Fig. 6c). Moreover, the SnO$_2$@TiO$_2$ composite also shows the much better cycling performance and higher lithium storage compared to the SnO$_2$@TiO$_2$ double-shell nanotubes (300 mAh g^{-1} after 50 cycles at 800 mA g^{-1}) [22]. Obviously, these capacities are higher than the values observed in SnO$_2$ NPs and reported practical capacity of TiO$_2$ (150–170 mAh g^{-1}) [31,32]. We suggest that the high capacity of SnO$_2$ and the superior cycling performance of TiO$_2$ are synergistically combined in the SnO$_2$@TiO$_2$ composite electrode [22]. Fig. 6d shows the rate capability of the SnO$_2$@TiO$_2$ composite electrode at various current densities from 200 to 2000 mA g^{-1}. The specific discharge capacities of the composite are about 520, 400, 304, 222,

204 mAh g^{-1} when cycles at 200, 400, 800, 1600, 2000 mA g^{-1}, respectively. When back to 200 mA g^{-1}, a capacity of 450 mAh g^{-1} can be restored, indicating the good rate performance of the SnO$_2$@TiO$_2$ composite. And then, the electrode continues to discharge/charge cycling at 2000 mA g^{-1} after rate test, and delivers a discharge capacity of 201 mAh g^{-1} after 500 cycles (inset in Fig. 6d), further indicating the excellent cycling performance of the SnO$_2$@TiO$_2$ composite.

The outstanding electrochemical performance of the SnO$_2$@TiO$_2$ composite electrode can be attributed to its unique architecture with hollow TiO$_2$ nanowires shell encapsulating SnO$_2$ NPs cores, which intrinsically possesses void space in between the TiO$_2$ shell and SnO$_2$ NPs cores, facilitating lithium ion diffusion, providing space for the free expansion of SnO$_2$, and further, effective mechanical support from the TiO$_2$ shell, alleviating the stress that is created during discharge/charge cycling, preventing the pulverization of SnO$_2$ nanoparticles and maintaining the structural integrity. The superiorities of SnO$_2$@TiO$_2$ composite mentioned above, contributing to enhanced lithium storage performance.

To confirm the structural integrity of the SnO$_2$@TiO$_2$ electrode during repeated cycling, we decomposed two cells after 200 cycles and 500 cycles at a current density of 800 mA g^{-1}, respectively, and the electrode was observed using TEM. Fig. 7a, b shows that the curved wires-like 1-D structure was still preserved after 200 cycles at 800 mA g^{-1}, but the primary distinct void space between shell and cores became narrow and obscure due to the volume expansion of SnO$_2$ during cycling. Furthermore, we found that the nanowire morphology was still preserved even after 500 cycles but the void space was completely lost (Fig. 7c, d). These observations confirmed that encapsulation of SnO$_2$ nanoparticles into hollow TiO2 nanowires and intrinsical possession of void space in between the TiO$_2$ shell and SnO$_2$ NPs cores were very effective for accommodating the large volume expansion of SnO$_2$ and maintaining the structural integrity, which brought stable cyclability and good lithium storage performance.
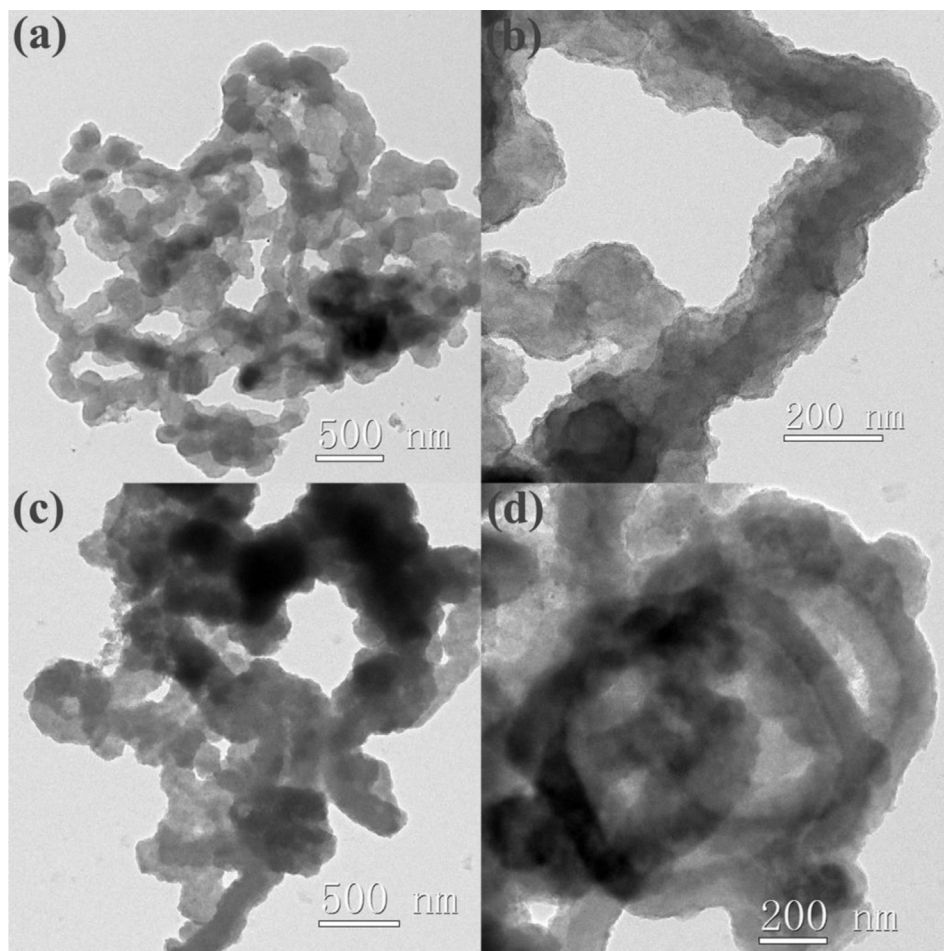
Fig. 7. TEM images of SnO$_2$@TiO$_2$ composite after different cycle number at 800 mA g^{-1}: (a) TEM image and (b) magnified TEM image after 200 cycles, (c) TEM image and (d) magnified TEM image after 500 cycles.

4. Conclusions

In summary, we have successfully prepared SnO$_2$@TiO$_2$ composite, namely encapsulation of SnO$_2$ nanoparticles into hollow TiO$_2$ nanowires. The TiO$_2$ shell of SnO$_2$@TiO$_2$ composite, which possesses neglectable volume change (3–4%) not only alleviates the pulverization and drastic volume change of the SnO$_2$ NPs and maintains the structural integrity, but also contributes to the total capacity of the composite. This unique structure possesses built-in void space in between the TiO$_2$ shell and SnO$_2$ NPs core, which not only allow for the free expansion of SnO$_2$ without rupturing the hollow TiO$_2$ nanowires shell but also enable the formation of highly efficient channels for the fast transport of both electrons and lithium ion during discharge/charge cycling process. As a result, the as-prepared SnO$_2$@TiO$_2$ composite delivered a reversible discharge capacity of 445 and 200 mAh g^{-1} after 500 cycles at a current density of 800 and 2000 mA g^{-1}, respectively. Thus, the SnO$_2$@TiO$_2$ composite exhibits good lithium ion storage capacity and excellent cycling performance, which are mainly attributed to the unique architecture of hollow TiO$_2$ nanowires shell encapsulating SnO$_2$ NPs cores.

Acknowledgments

Appendix A. Supplementary data

Supplementary data related to this article can be found at http://dx.doi.org/10.1016/j.jpowsour.2013.12.049.

References

[1] Z.X. Yang, G.D. Du, Z.P. Guo, X.B. Yu, Z.X. Chen, T.L. Guo, R. Zeng, Nanoscale 3 (2011) 4440.
[2] Z.H. Wen, G.H. Lu, S. Mao, H. Kim, S.M. Cui, K.H. Yu, X.K. Huang, P.T. Hurley, O. Mao, J.H. Chen, Electrochem. Commun. 29 (2013) 67.
[3] P. Poizot, S. Laruelle, S. Grugeon, L. Dupont, J.M. Tarascon, Nature 407 (2000) 496.
[4] F.Y. Cheng, J. Liang, Z.L. Tao, J. Chen, Adv. Mater. 23 (2011) 1695.
[5] S.J. Han, B.C. Jang, T. Kim, S.M. Oh, T. Hyeon, Adv. Funct. Mater. 15 (2005) 1845.
[6] X.W. Low, Y. Wang, C. Yuan, J.Y. Lee, L.A. Archer, Adv. Mater. 18 (2006) 2325.
[7] S.J. Ding, J.S. Chen, X.W. Lou, Chem. Asian J. (2011) 2278–2281.
[8] Y. Wang, M.H. Wu, Z. Jiao, J.Y. Lee, Nanotechnology 20 (2009) 7.
[9] Z.Y. Wang, D.Y. Luan, Freddy Yin Chiang Boey, X.W. (David) Lou, J. Am. Chem. Soc. 133 (2011) 4738–4741.
[10] C. Wang, G.H. Du, K. Stahl, H.X. Huang, Y.J. Zhong, J.Z. Jiang, J. Phys. Chem. C 116 (2012) 4000.
[11] H.X. Zhang, C. Feng, Y.C. Zhai, K.L. Jiang, Q.Q. Li, S.S. Fan, Adv. Mater. 21 (2009) 2299.
[12] L.P. Zhao, L. Gao, Carbon 42 (2004) 1858.
[13] G. Chen, Z.Y. Wang, D.G. Xia, Chem. Mater. 20 (2008) 6951.
[14] J. Zhu, D.N. Lei, G.H. Zhang, Q.H. Li, B.G. Lu, T.H. Wang, Nanoscale 5 (2013) 5499.
[15] C.H. Xu, J. Sun, L. Gao, J. Phys. Chem. C 113 (2009) 20509.
[16] P. Wu, N. Du, H. Zhang, J.X. Yu, D.R. Yang, J. Phys. Chem. C 114 (2010) 22535–22538.
[17] Z.H. Wen, Q. Wang, Q. Zhang, J.H. Li, Adv. Funct. Mater. 17 (2007) 2772.
[18] L. Shen, X. Zhang, H. Li, Y. Zhao, F. Bijarbooneh, V. Malgras, Y. Lee, Y.M. Kang, S.X. Dou, J. Am. Chem. Soc. 133 (2011) 19314–19317.

[19] H.L. Jiang, X.L. Yang, C. Chen, Y.H. Zhu, C.Z. Li, New J. Chem. 37 (2013) 1578.
[20] W.W. Zhou, Y.Y. Tay, X.T. Jia, D.Y.Y. Wai, J. Jiang, H.H. Hoon, T. Yu, Nanoscale 4 (2012) 4459.
[21] C. Li, W. Wei, S. Fang, H. Wang, Y. Zhang, Y. Cui, R. Chen, J. Power Sources 195 (2010) 2939.
[22] J.H. Jeun, K.Y. Park, D.H. Kim, W.S. Kim, H.C. Kim, B.S. Lee, H. Kim, W.R. Yu, K. Kang, S.H. Hong, Nanoscale 5 (2013) 8480.
[23] J. Ye, H. Zhang, R. Yang, X. Li, L. Qi, Small 6 (2010) 296.
[24] J.S. Chen, Y.L. Cheah, Y.T. Chen, N. Layaprakash, S. Madhavi, H.Y. Yang, X.W. Lou, J. Phys. Chem. C 113 (2009) 20504.
[25] J.S. Chen, Y.L. Tan, C.M. Li, Y.L. Cheah, D.Y. Luan, S. Madhavi, F.Y.C. Boey, L.A. Archer, X.W. Lou, J. Am. Chem. Soc. 132 (2010) 6124.
[26] S.J. Ding, J.S. Chen, G.G. Qi, X.N. Duan, Z.Y. Wang, E.P. Giannelis, L.A. Archer, X.W. Lou, J. Am. Chem. Soc. 133 (2011) 21.
[27] Y. Qiao, X.L. Hu, Y. Liu, C.J. Chen, H.H. Xu, D.F. Hou, P. Hu, Y.H. Huang, J. Mater. Chem. A 1 (2013) 10378.
[28] Y.M. Li, X.J. Lv, J. Lu, J.H. Li, J. Phys. Chem. C 114 (2010) 21771.
[29] M.M. Liu, X.W. Li, H. Ming, J. Adkins, X.W. Zhao, L.L. Su, Q. Zhou, J.W. Zheng, New J. Chem. 37 (2013) 2098.
[30] X.W. Lou, C.M. Li, L.A. Archer, Adv. Mater. 21 (2009) 2536–2539.
[31] D. Deng, M.G. Kim, J.Y. Lee, J. Cho, Energy Environ. Sci. 2 (2009) 818.
[32] Y.S. Hu, L. Kienie, Y.G. Guo, J. Maier, Adv. Mater. 18 (2006) 1421.